Electronic Supplementary Information

Phase Formation and Photocatalytic Properties of Chalcostibite and Tetrahedrite Thin Films Derived from Copper and Antimony Xanthates

Marco Sigl,[a] Melissa Egger,[a] Daniel Knez,[b] Stephen Nagaraju Myakala,[c] Connor M. J. Marshall,[d] Joe Kaye,[d] Ali Salehi-Reyhani,[e] Heinz Amenitsch,[f] Alexey Cherevan,[c] Dominik Eder,[c] Gregor Trimmel,[a] Saif A. Haque,[d] Thomas Rath[a,]*

[a] Institute for Chemistry and Technology of Materials, NAWI Graz, Graz University of Technology, Stremayrgasse 9, 8010 Graz, Austria. *corresponding author E-mail: thomas.rath@tugraz.at

[b] Institute of Electron Microscopy and Nanoanalysis, Graz University of Technology, Steyrergasse 17, 8010 Graz, Austria

[c] Institute of Materials Chemistry, TU Wien, Getreidemarkt 9, 1060 Vienna, Austria

[d] Department of Chemistry, Molecular Sciences Research Hub, Imperial College London, White City Campus, 82 Wood Lane, W12 0BZ London, UK

[e] Department of Surgery and Cancer, Imperial College London, London, W12 0HS, UK

[f] Institute of Inorganic Chemistry, NAWI Graz, Graz University of Technology, Stremayrgasse 9, 8010 Graz, Austria

Copper *O*-2,2-dimethylpenthan-3-yl dithiocarbonate

The copper xanthate was synthesized according to a previously reported study:[1]

Potassium tert-butoxide (1.0 equiv.) was dissolved in THF in inert atmosphere. The solution was cooled to 0 °C, then 1.1 equiv. 2,2-dimethyl-3-pentanol were slowly added. After stirring for a few minutes, CS_2 (1.1 equiv.) was added dropwise and the solution was stirred for about 5 hours. The reaction mixture was diluted with diethyl ether. The solid obtained by filtration was dried in vacuum and afterwards dissolved in acetone to separate insoluble side products. The acetone solution was concentrated by rotary evaporation and then the product was precipitated by addition of diethyl ether. The product was separated by filtration and dried under vacuum to give a white-yellowish powder.

Copper (II) chloride dihydrate (23.7 mmol, 1 equiv.) was dissolved in 50 mL of deion. water. A solution of potassium xanthate (52.1 mmol, 2.2 equiv.) in 150 mL of deion. water was added dropwise to the copper chloride solution under vigorous stirring. The reaction was stirred for about 5 hours, then the water was decanted off and the residue was dried in vacuum. The residue was dissolved in chloroform and added to methanol to precipitate a yellow powder, which was dried under vacuum. Afterwards, this powder was washed in n-pentane and dried in vacuum to obtain the yellow copper xanthate.

^1H NMR shift (ppm): 5.24 (**A**, t, 1H), 1.72 (**B**, p, 2H), 0.96 (**C**, m, 12H)

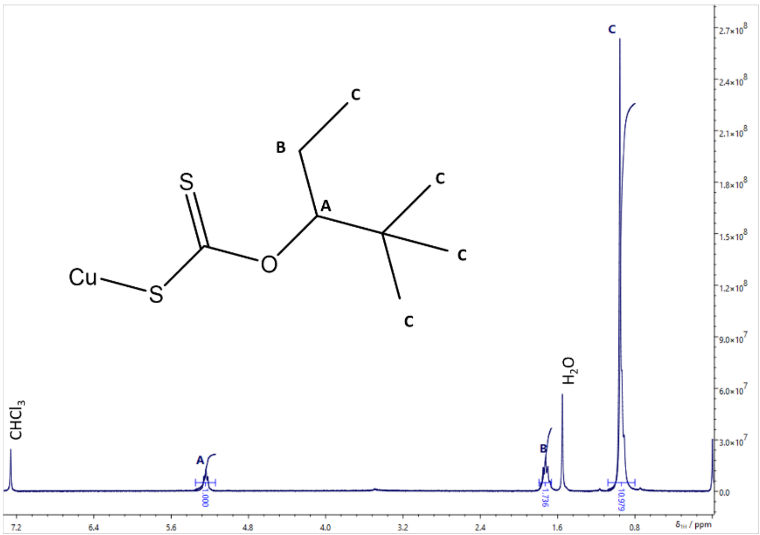

Fig. S1 *^1H NMR spectrum of the purified copper xanthate.*

Antimony (III) *O*-propan-2-yl dithiocarbonate

The antimony xanthate was synthesized according to a previously reported procedure:[2]

Potassium hydroxide was stirred in a 1 : 1 molar ratio with 2-propanol. The solution was cooled in an ice bath followed by a dropwise addition of carbon disulfide to a slight excess (7.4 mmol, 1.1 equiv.). The resulting slurry was stirred for 30 min before vacuum filtering and washing with diethyl ether. The potassium *O*-propan-2-yl dithiocarbonate was then recrystallized from methanol. To form the antimony xanthate, an aqueous solution of $SbCl_3$ (acidified with HCl conc.; 11 mL/g of $SbCl_3$ were used to facilitate dissolution of $SbCl_3$) was added to a rapidly stirred aqueous solution of the potassium xanthate in a molar ratio of 1 : 3 and stirred for 60 min at room temperature. The pale-yellow product was filtered and washed with water followed by methanol. The product was then recrystallized from acetone and dried in vacuum.

^{1}H NMR shift (ppm): 5.59 (A, sep, 1H), 1.44 (B, d, 6H)

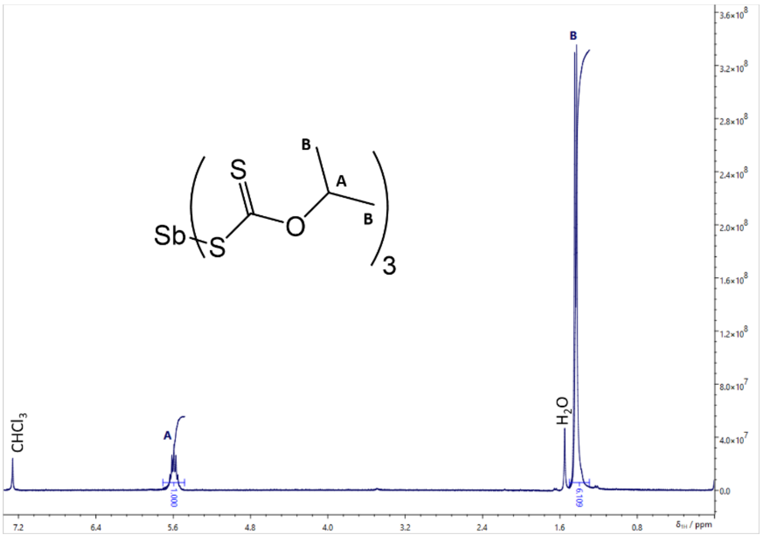

Fig. S2 *^{1}H NMR spectrum of the purified antimony xanthate.*

Kubelka-Munk equation and Tauc plot:

$$F(R_\infty) = \frac{K}{S} = \frac{(1-R_\infty)^2}{2R_\infty} \qquad \textit{Equation S1}$$

where $R_\infty = R_{sample}/R_{standard}$ and describes an infinitely thick specimen and K and S are the absorption and scattering coefficients, respectively.[3–6]

In the Tauc method

$$(\alpha * h\upsilon)^{1/\gamma} = B(h\upsilon - E_g) \qquad \textit{Equation S2}$$

α can be exchanged with $F(R_\infty)$ to obtain

$$(F(R_\infty) * h\upsilon)^{1/\gamma} = B(h\upsilon - E_g) \qquad \textit{Equation S3}$$

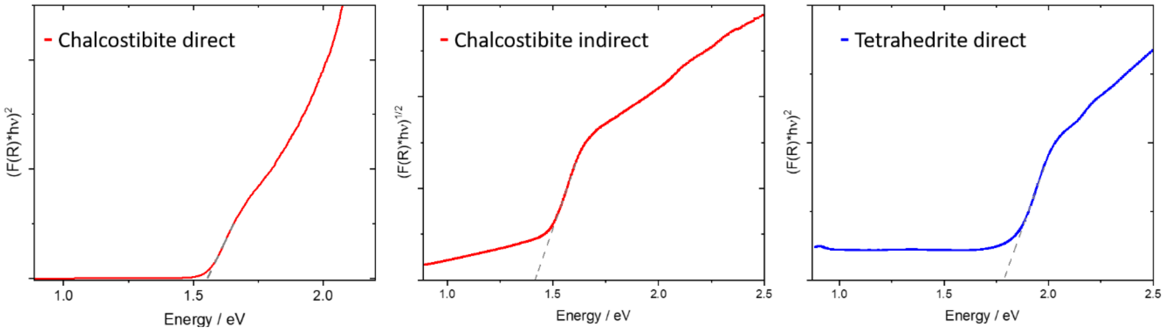

Fig. S3 *Tauc plots from the Kubelka-Munk method for chalcostibite (direct and indirect bandgap), as well as for tetrahedrite for a direct bandgap.*

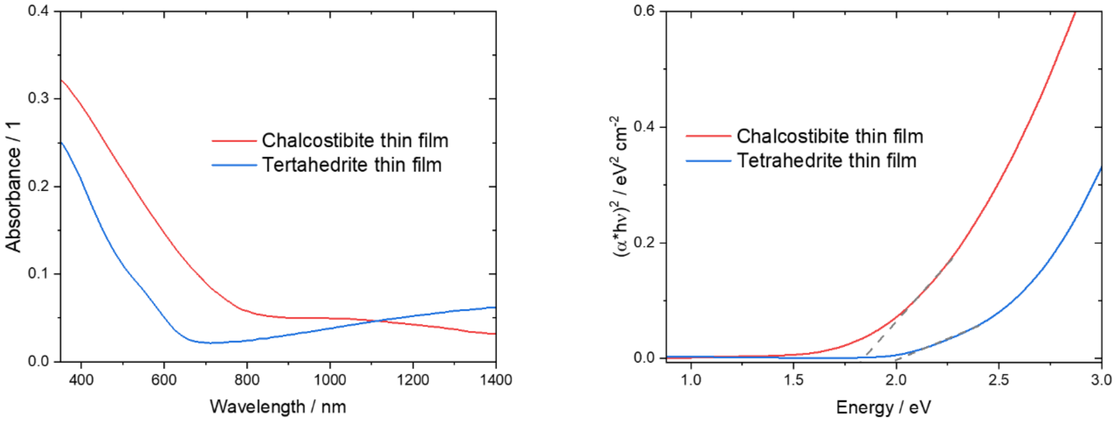

Fig. S4 *UV-vis absorption spectra and Tauc plots of the copper antimony sulfide thin films (thickness: 80 nm).*

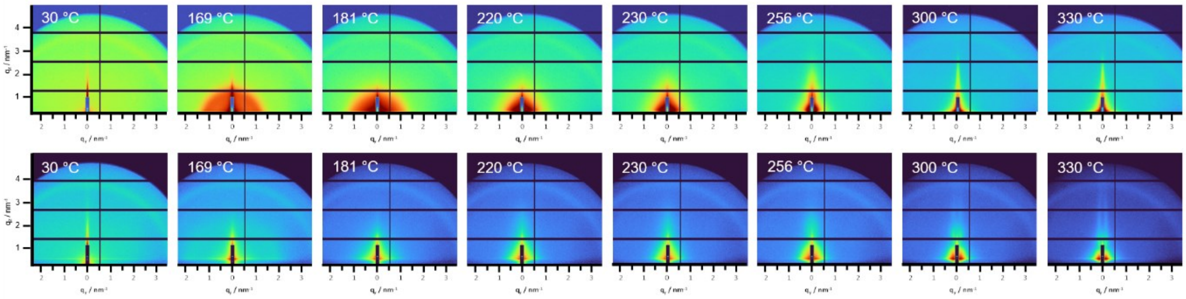

Fig. S5 *2D GISAXS images measured at certain temperatures during the heating run: chalcostibite (top line), tetrahedrite (bottom line).*

GISAXS data fitting

We fitted the in-plane line-cuts according to:
$I_{calc}(q) = a * F(q) *S_{SHS}(q) + I_{Porod}(q) + BG$

- a describes an intensity scalar
- F(q) describes the form-factor scattering
- $S_{SHS}(q)$ describes the structure-factor contribution (Sticky hard sphere)
- $I_{Porod}(q)$ describes the Porod-contribution resulting from large scale aggregates
- BG describes the background

The first curve of each heating run was fitted with a 6th order polynomial and used as a background for the fitting of the fully converted materials (**Fig. S6**, black curves). An analytical expression for polydisperse Schultz-distributed spheres is used to describe the form-factor and the structure factor is described by a sticky hard sphere model. More details to the fitting function and fitted parameters can be found in the publications of Pontoni et al. (2003)[7], Sharma et al. (1977)[8], Kotlarchyk et al. (1988)[9] and Rigodanza et al. (2021).[10]

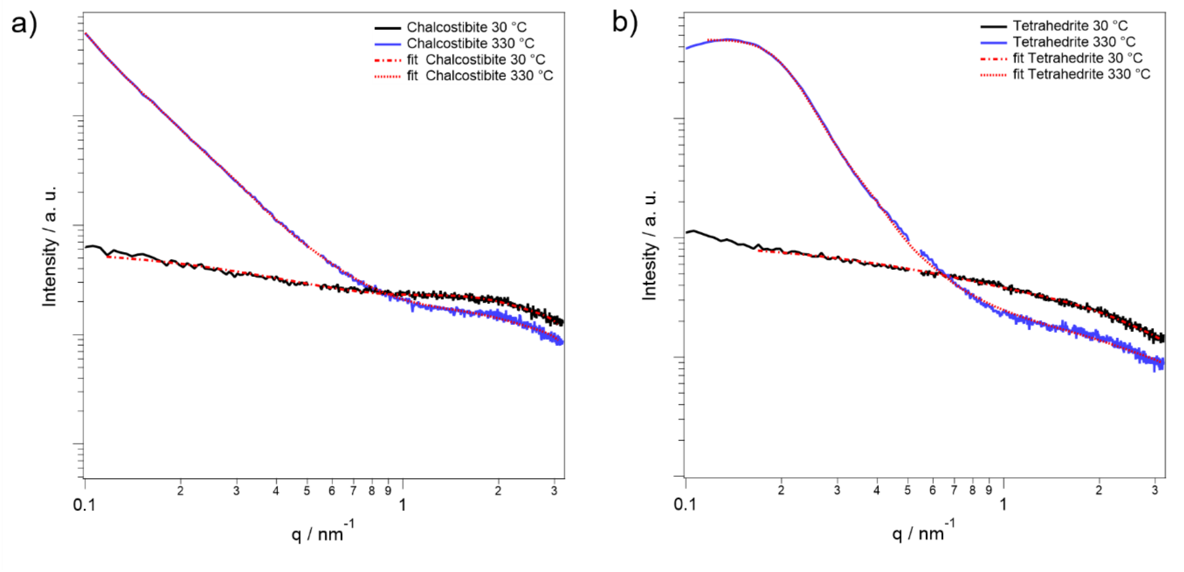

***Fig. S6** Line-cuts of a) chalcostibite and b) tetrahedrite samples at 30 °C (black) and 330 °C (blue) with the corresponding fitted curves in red.*

***Table S1** Fitting parameters obtained for chalcostibite and tetrahedrite films with a short description.*

Parameter	**Chalcostibite**	**Tetrahedrite**	**Description**
BG	1.15 ± 0.26	3.31 ± 0.23	Background
I_{sph}	(70.6 ± 6.0) x 10^3 *	(12.44 ± 0.38) x 10^3	Scattering intensity
R_{sph}	31.99 ± 0.32 *	7.3 ± 0.14	Schultz sphere-radius (pore-sizes)
sig_{sph}	5.76 ± 0.36 *	3.01 ± 0.04	Deviation of the pore-sizes
R_{HS}	10.00 ± 0.14 *	15.117 ± 0.053	Hard-sphere radius
p_{HS}	0.226 ± 0.001 *	0.155 ± 0.002	Volume fraction
λ_{HS}	0.1 (constant)	0.1 (constant)	Relative potential well size $\lambda_{HS} = 0.1$ ($\lambda = 1 + \lambda_{HS}$)
ε_{HS}	0 (constant)	0 (constant)	Relative potential well depth
c_p	5.480 ± 0.074	4.6 ± 2.0	Porod constant
p	2.962 ± 0.009	1.54 ± 0.46	Power law exponent
c_{pol}	0.610 ± 0.014	0.367 ± 0.052	Portion of the fitted background

* values fitted outside of the available q-range and thus not significant.

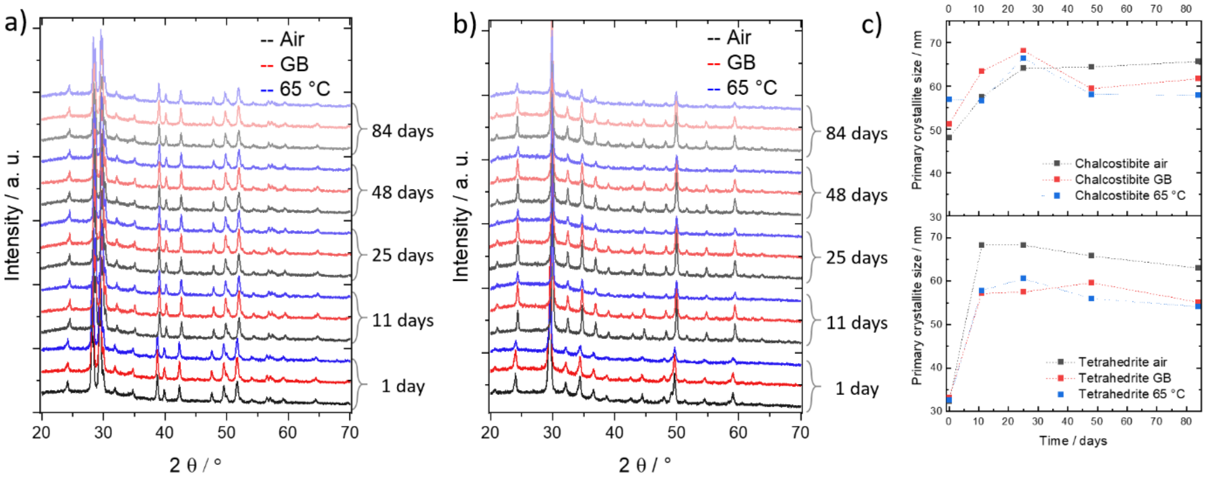

Fig. S7 *XRD patterns of (a) chalcostibite and (b) tetrahedrite thin films stored in different conditions (ambient air, under nitrogen in a glovebox at room temperature, under nitrogen in a glovebox at 65 °C) recorded after 1, 11, 25, 48 and 84 days. The patterns are shifted for better visibility; c) Estimated primary crystallite sizes extracted from the diffractograms using the Scherrer equation for both phases over 84 days.*

Photocatalytic dye degradation tests

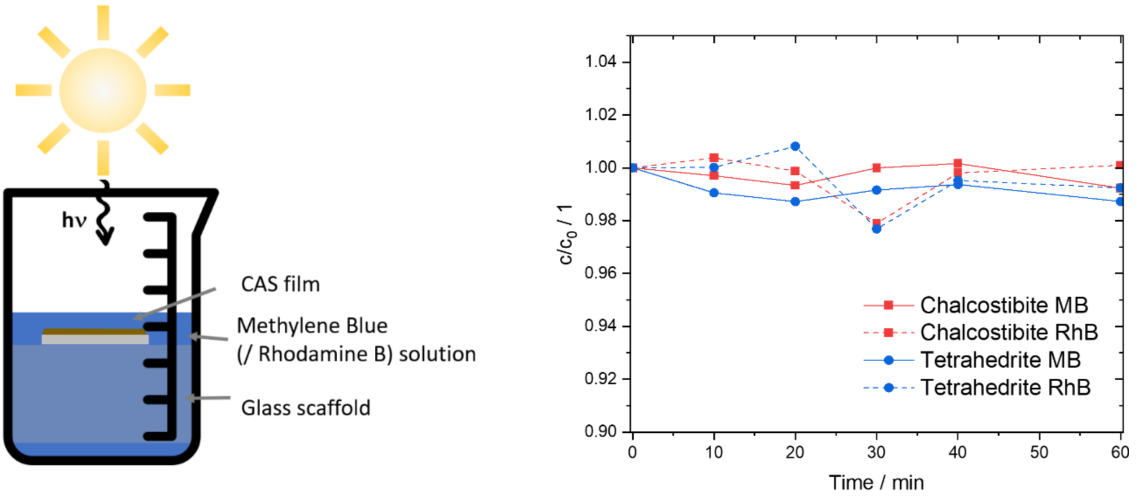

Fig. S8 *Set-up used for the photocatalytic dye degradation experiments (left) and relative concentration over time during the adsorption phase (right).*

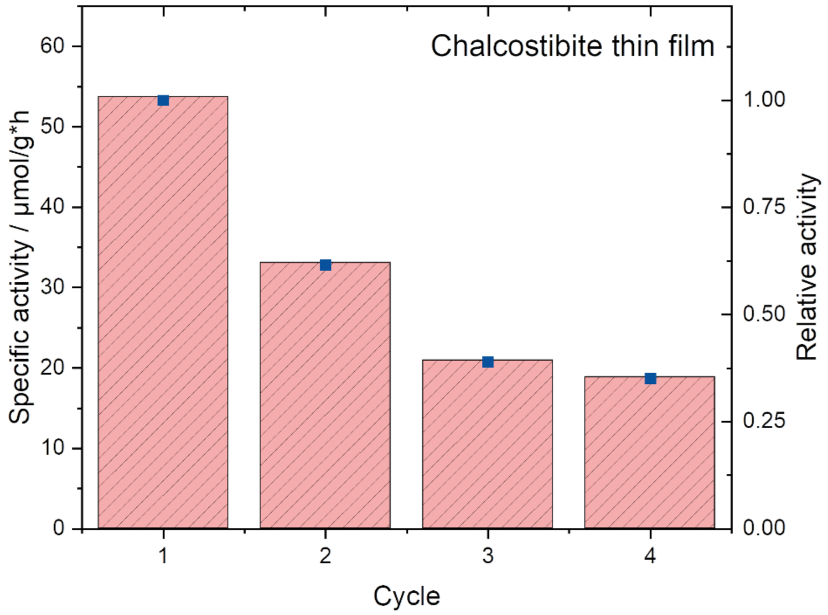

Fig. S9 *Specific activity (photocatalytic MB degradation) of chalcostibite thin films over several cycles.*

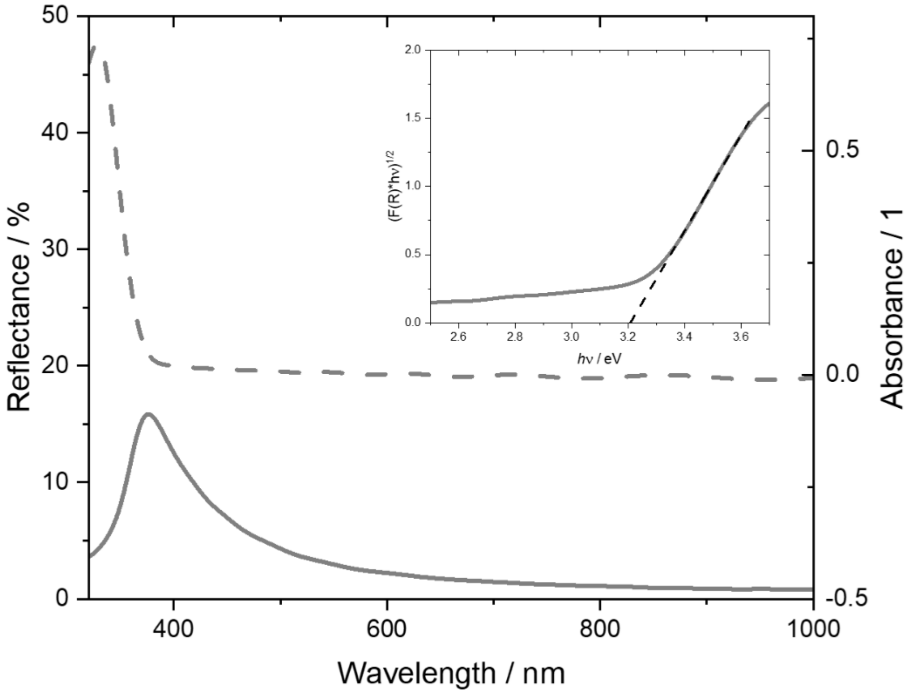

Fig. S10 *Diffuse reflectance and absorption spectra of a mp-TiO_2 thin film and the band gap determination via the Kubelka-Munk method (inset).*

Spin-trap EPR measurements

DMPO (5,5-Dimethyl-1-pyrroline N-oxide) was used as the spin trap. Glass samples were placed in standard 5 mm NMR tubes and filled with a 200 mM toluene solution of the spin trap, prepared to be free of background EPR signals. The samples were irradiated for 120 sigh-intensity LED photoreactor operating at 405 nm. EPR spectra were recorded at room temperature using a MiniScope MS300 X-band EPR spectrometer (Magnetech). The time between irradiation and completion of the EPR spectrum acquisition was approximately 5-6 minutes.

The copper antimony sulfide thin films were prepared analogous to the other investigations with a spin coating speed of 1500 rpm (ramp: 1500 rpm/s) for 30 s, but using 0.1 mm glass slides. Smaller parts of the coated glass slides were placed in NMR tubes with a 200 mM solution of DMPO (5,5’-dimethyl-1-pyrroline N-oxide). The DMPO solution alone was EPR-silent. However, upon irradiation at 405 nm for 120 s, distinct EPR signals emerged.

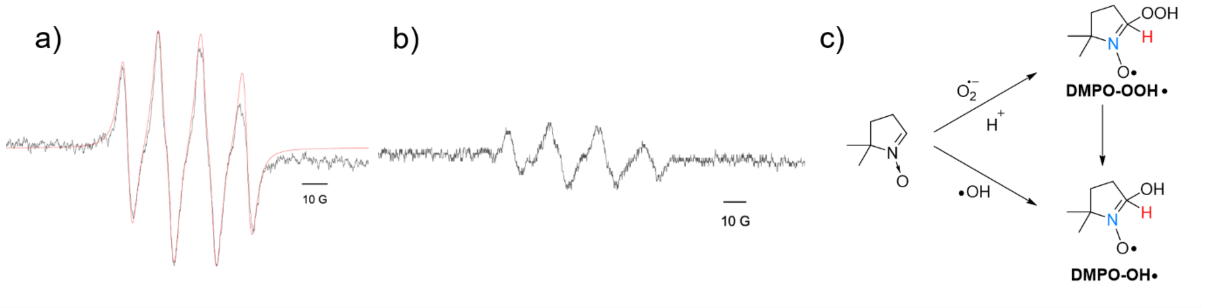

Fig. S11 *EPR spectra obtained after the irradiation (405 nm, 120 s) of a) tetrahedrite and b) chalcostibite with DMPO as spin-trap in the presence of atmospheric oxygen (black lines). The red line shows the simulated EPR spectrum (a_N = 13.5 G, a_H = 12 G); c) Reactions between DMPO and superoxide and hydroxyl radicals. Nuclei with observable EPR hyperfine coupling constants are shown in color.*

Photocatalytic hydrogen evolution tests

The photocatalytic experiments were carried out in a custom-built closed reactor setup (total volume of 32 mL) equipped with a water-cooling jacket maintained at 15 °C throughout the experiment to maintain a constant temperature. The reactor was illuminated from the side using a monochromatic UV LED light source centered at 365 ± 6 nm with an intensity of 238 mW.cm^{-2}. Briefly, the reactor was filled with 7. 5 mL DI H_2O and 5 mL of HPLC CH_3OH, followed by carefully placing the catalyst film inside the reactor. The reactor was then purged with argon for 10 min at 10 mL min^{-1} to remove any dissolved oxygen from the reaction solution and reactor headspace. Following this, the catalyst film was illuminated for a total of 2 h, sampling 300 µL of the headspace at different time intervals. H_2 produced was quantified via gas chromatography (Shimadzu GC 2030) equipped with a barrier ionization discharge detector and a Micropacked-ST column with He (6.0) as the carrier gas, calibrated using a 5-point calibration.

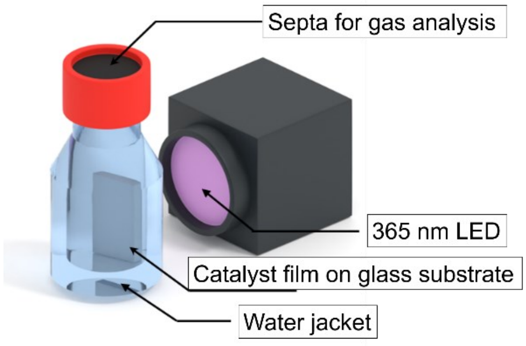

Fig. S12 *Schematic illustration of the set-up used for the hydrogen evolution experiments.*

ppm to µmoL conversion:

Based on the headspace of the reactor, the total amount of H_2 present in the gas phase is, H_2 (in ppm) x 10^{-6} x headspace (mL). Assuming ideal gas behavior, 1 mole of H_2 occupies a volume of 23632.5 mL at 1 atm, 288 K. Therefore, the total moles of H_2 produced are given by

$$H_2(mol) = \frac{(H_2(in\ ppm) * 10^{-6} * headspace(mL))}{23632.5} \qquad \textit{Equation S4}$$

Table S2 *Comparison of photocatalytic activities with materials from the literature*

catalyst	**dye**	**specific activity / µmol/g*h**	**publication**
Chalcostibite	MB	52	This work
Tetrahedrite	MB	31	
TiO$_{2m}$	MB	11	
Chalcostibite @ TiO$_{2m}$	MB	18	
Tetrahedrite @ TiO2$_{m}$	MB	8.9	
Zn-doped CuS	MB	75	Cao et al. 2024[11]
CuS modified TiO$_2$	MB	75	El-Gendy et al. 2023[12]
MoS$_2$ modified TiO$_2$	MB	78	
MoS$_2$ and N modified TiO$_2$	MB	40	Sharkawy et al. 2023[13]
TiO$_{2m}$	RhB	12	This work
Chalcostibite @ TiO$_{2m}$	RhB	13	
Tetrahedrite @ TiO2$_{m}$	RhB	11	
ZnIn$_2$S$_4$ thin film	RhB	78	Sigl et al. 2024[14]
ZnIn$_2$S$_4$ microspheres	RhB	7.0	Chen et al. 2009[5]
Sm-doped ZnIn$_2$S$_4$ microspheres	RhB	58	Tan et al. 2014[15]
CuSbS$_2$–CdS–ZnO	RhB	38	Wang et al. 2023[16]
		specific activity / mmol/g*h	
Chalcostibite @ mp-TiO$_2$	H$_2$ evolution	0.75	This work
Tetrahedrite @ mp-TiO$_2$	H$_2$ evolution	2.6	
Rod-like CuSbS$_2$	H$_2$ evolution	0.628	Sarilmaz et al. 2020[17]
Nanocrystalline CusbS$_2$	H$_2$ evolution	0.274	
CuSbS$_2$-CdS-ZnO	H$_2$ evolution	0.042	Wang et al. 2023[16]
ZnIn$_2$S$_4$/In(OH)$_3$/ZnWO$_4$	H$_2$ evolution	1.03	Zhao et al. 2018[18]
Co-TiO$_2$	H$_2$ evolution	1.16	Tran et al. 2012[19]
CNT-Cd$_{0.1}$Zn$_{0.9}$S	CNT-Cd$_{0.1}$Zn$_{0.9}$S	1.56	Yu et al. 2012[20]

References

1 T. Rath, M. Edler, W. Haas, A. Fischereder, S. Moscher, A. Schenk, R. Trattnig, M. Sezen, G. Mauthner, A. Pein, D. Meischler, K. Bartl, R. Saf, N. Bansal, S. A. Haque, F. Hofer, E. J. List and G. Trimmel, *Adv. Energy Mater.*, 2011, **1**, 1046–1050.

2 T. Rath, A. J. MacLachlan, M. D. Brown and S. A. Haque, *J. Mater. Chem. A.*, 2015, **3**, 24155–24162.

3 P. Kubelka and F. Munk, *Z. Tech.Phys.*, 1931, **12**, 593–601.

4 R. López and R. Gómez, *J. Sol.-Gel. Sci. Technol.*, 2012, **61**, 1–7.

5 Z. Chen, D. Li, W. Zhang, Y. Shao, T. Chen, M. Sun and X. Fu, *J. Phys. Chem. C*, 2009, **113**, 4433–4440.

6 S. S. Abdullahi, S. Güner, Y. Koseoglu, I. M. Musa, B. I. Adamu and M. Abdulhamid, *J. Niger. Assoc. Math. Phys.*, 2016, **35**, 241–246.

7 D. Pontoni, S. Finet, T. Narayanan and A. R. Rennie, *J. Chem. Phys.*, 2003, **119**, 6157–6165.

8 R. V. Sharma and K. C. Sharma, *Physica A*, 1977, **89**, 213–218.

9 M. Kotlarchyk, R. B. Stephens and J. S. Huang, *J. Phys. Chem.*, 1988, **92**, 1533–1538.
10 F. Rigodanza, M. Burian, F. Arcudi, L. Đorđević, H. Amenitsch and M. Prato, *Nat. Commun.*, 2021, **12**, 2640.
11 J. Cao, D. Zhang and H. Zhang, *Mater. Res. Bull.*, 2024, **179**, 112990.
12 R. A. El-Gendy, H. M. El-Bery, M. Farrag and D. M. Fouad, *Sci. Rep.*, 2023, **13**, 7994.
13 H. M. El Sharkawy, A. M. Shawky, R. Elshypany and H. Selim, *Sci. Rep.*, 2023, **13**, 8845.
14 M. Sigl, M. Egger, F. Warchomicka, D. Knez, M. Dienstleder, H. Amenitsch, G. Trimmel and T. Rath, *J. Mater. Chem. A*, 2024, **12**, 28965–28974.
15 C. Tan, G. Zhu, M. Hojamberdiev, K. S. Lokesh, X. Luo, L. Jin, J. Zhou and P. Liu, *J. Hazard. Mater.*, 2014, **278**, 572–583.
16 W. Wang, Q. Sheng, G. Zhi, Y. Zhao, R. Qu, L. Sun and S. Zhang, *Appl. Surf. Sci.*, 2023, **639**, 158251.
17 A. Sarilmaz, E. Genc, E. Aslan, A. Ozen, G. Yanalak, F. Ozel and I. H. Patir, *J. Photochem. Photobiol. A,* 2020, **400**, 112706.
18 J. Zhao, X. Yan, N. Zhao, X. Li, B. Lu, X. Zhang and H. Yu, *RSC Adv.*, 2018, **8**, 4979–4986.
19 P. D. Tran, L. Xi, S. K. Batabyal, L. H. Wong, J. Barber and J. S. C. Loo, *Phys. Chem. Chem. Phys.*, 2012, **14**, 11596–11599.
20 J. Yu, B. Yang and B. Cheng, *Nanoscale*, 2012, **4**, 2670–2677.